JACS Au
AN OPEN ACCESS JOURNAL OF THE AMERICAN CHEMICAL SOCIETY

pubs.acs.org/jacsau

Article

New Magic Au_{24} Cluster Stabilized by PVP: Selective Formation, Atomic Structure, and Oxidation Catalysis

Shingo Hasegawa, Shinjiro Takano, Koji Harano, and Tatsuya Tsukuda*

Cite This: *JACS Au* 2021, 1, 660–668

Read Online

ACCESS | Metrics & More | Article Recommendations | Supporting Information

ABSTRACT: An unprecedented magic number cluster, $Au_{24}Cl_x$ (x = 0–3), was selectively synthesized by the kinetically controlled reduction of the Au precursor ions in a microfluidic mixer in the presence of a large excess of poly(*N*-vinyl-2-pyrrolidone) (PVP). The atomic structure of the PVP-stabilized $Au_{24}Cl_x$ was investigated by means of aberration-corrected transmission electron microscopy (ACTEM) and density functional theory (DFT) calculations. ACTEM video imaging revealed that the $Au_{24}Cl_x$ clusters were stable against dissociation but fluctuated during the observation period. Some of the high-resolution ACTEM snapshots were explained by DFT-optimized isomeric structures in which all the constituent atoms were located on the surface. This observation suggests that the featureless optical spectrum of $Au_{24}Cl_x$ is associated with the coexistence of distinctive isomers. X-ray photoelectron spectroscopy and Fourier-transform infrared spectroscopy of CO adsorbates revealed the electron-rich nature of $Au_{24}Cl_x$ clusters due to the interaction with PVP. The $Au_{24}Cl_x$:PVP clusters catalyzed the aerobic oxidation of benzyl alcohol derivatives without degradation. Hammett analysis and the kinetic isotope effect indicated that the hydride elimination by $Au_{24}Cl_x$ was the rate-limiting step with an apparent activation energy of 56 ± 3 kJ/mol, whereas the oxygen pressure dependence of the reaction kinetics suggested the involvement of hydrogen abstraction by coadsorbed O_2 as a faster process.

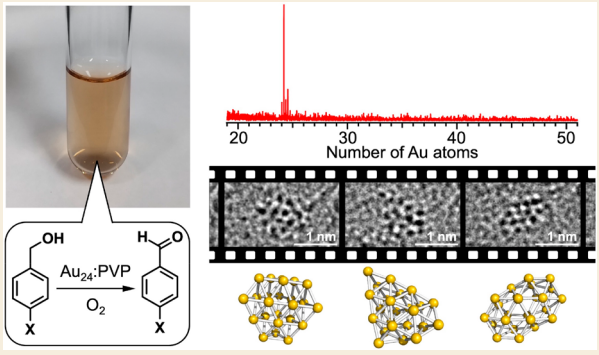

KEYWORDS: *magic number gold cluster, poly(N-vinyl-2-pyrrolidone), isomerization, aerobic alcohol oxidation, aberration-corrected transmission electron microscopy, density functional theory calculation*

INTRODUCTION

Metal clusters with diameters smaller than the critical dimension of ∼2 nm are known to show unique chemical reactivities that cannot be predicted by a simple scaling law deduced from those of the extended surfaces and nanoparticles (NPs) of the corresponding metal.[1−10] The emergence of the novel catalytic properties in metal clusters is ascribed to the quantized electronic structures, specific surface structures, and structural fluxionality. To understand the origin of novel catalysis and to optimize the catalytic performances of metal clusters, it is crucial to control their sizes with atomic precision. Atomically precise synthesis of Au clusters has been achieved using protecting ligands such as thiolates, alkynyls, halides, phosphines, and *N*-heterocyclic carbenes.[2,3,11] Successful synthesis relies on size-focusing by chemical etching and subsequent isolation by chromatography and fractional precipitation. The main advantage of using atomically precise Au clusters for establishing the correlation between structures and catalytic performances is that their geometrical structures are determined by single-crystal X-ray diffraction (SCXRD).[2,3] Nevertheless, these ligand-protected Au clusters are in general not suitable for catalytic applications because all the surface atoms of the metal core are masked by the ligands, although ligand-induced promotion of catalysis has been reported for some reactions.[12]

For the catalytic application of metal clusters, stabilization by linear polymers is suitable, since the cluster surface is inevitably exposed owing to the steric repulsion between the polymers.[13−21] For example, it has been demonstrated that small (<3 nm) Au clusters stabilized by poly(*N*-vinyl-2-pyrrolidone) (PVP) show size-specific and high catalytic activities for oxidation and coupling reactions under aerobic conditions.[22−26] The average diameter of the Au NPs can be tuned using conventional wet-chemical methods such as seed-mediated growth.[27] It was reported that the catalytic activity of Au:PVP was monotonically enhanced with the decrease in the average diameter.[22,24] However, postsynthetic size-focusing methods,[2] size-selective fractionation,[28] and SCXRD are not applicable because of the weak Au−polymer interactions and polydisperse

Received: March 4, 2021
Published: April 14, 2021

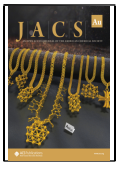

https://doi.org/10.1021/jacsau.1c00102
JACS Au 2021, 1, 660–668

structures of the polymer layers. Thus, major challenges for the catalytic studies of polymer-stabilized Au clusters are (1) atomically precise control of the cluster size and (2) determination of the atomic structure. The first challenge is tackled by controlling the formation kinetics of Au clusters in the presence of an excess amount of PVP using a microfluidic mixer,[29] followed by matrix-assisted laser desorption/ionization (MALDI) mass spectrometry. Previous studies have shown that Au:PVP prepared by microfluidic mixing were a mixture of magic number Au clusters such as $Au_{35\pm1}$, $Au_{43\pm1}$, and $Au_{58\pm1}$.[30,31] Therefore, there is a possibility of producing atomically precise Au:PVP through further control of the formation kinetics. The second issue can be addressed by using aberration-corrected transmission electron microscopy (ACTEM). A three-dimensional (3D) atomic structure can be determined from the 2D projection image with the help of density functional theory (DFT) calculations.[32,33] In addition, ACTEM video imaging with a high frame rate allows us to monitor the dynamic change in the structures at an atomic resolution.

In this study, we achieved atomically precise synthesis of an unprecedented magic number cluster, $Au_{24}Cl_x$, stabilized by PVP through the kinetically controlled reduction of Au precursor ions in the presence of a large amount of PVP. ACTEM video imaging with the help of DFT calculations revealed the coexistence of structural isomers in which all the Au atoms constituted the cluster surface. Au 4f X-ray photoelectron spectroscopy (XPS) and Fourier-transform infrared (FT-IR) spectroscopy of adsorbed CO indicated that $Au_{24}Cl_x$ was negatively charged. Kinetic studies were conducted for the aerobic oxidation of benzyl alcohol derivatives catalyzed by $Au_{24}Cl_x$. The clear kinetic isotope effect (KIE) and negative reaction constant in the Hammett plot indicated that the hydride elimination by $Au_{24}Cl_x$ was rate-limiting: the apparent activation energy was estimated to be 56 ± 3 kJ/mol by the Arrhenius equation. The reaction kinetics under pure oxygen (1 atm) suggested the involvement of direct hydrogen abstraction from adsorbed alkoxide by coadsorbed O_2. We believe that this work will open up a new research paradigm for atomically precise nanocatalysts.

RESULTS AND DISCUSSION

Atomically Precise Synthesis of $Au_{24}Cl_x$

Three samples of Au:PVP (**a**–**c**) were obtained at the [Au]:[PVP] mixing ratios of 1:40, 1:100, and 1:200, respectively. The size distributions of **a**–**c** were evaluated by MALDI mass spectrometry, based on our previous observations that Au clusters could be desorbed in the naked anionic form from the PVP matrix as a result of the MALDI processes.[30,31] Figure 1 shows typical MALDI mass spectra of **a**–**c** in the negative ion mode recorded under minimal laser fluence. Sample **a** contained $Au_{34}Cl_x^-$ (x = 0–4) and $Au_{43}Cl_x^-$ (x = 0–4), whereas sample **b** was a mixture of $Au_{24}Cl_x^-$ (x = 0–3), $Au_{33}Cl_x^-$ (x = 0–2), and $Au_{34}Cl_x^-$ (x = 0–3). Most notably, the mass spectrum of sample **c** is dominated by the progression of peaks assigned to $Au_{24}Cl_x^-$ (x = 0–3). According to classical nucleation theory,[34] formation of atomically monodisperse Au clusters in sample **c** is attributed to a kinetically controlled nucleation of Au atoms and a suppression of the subsequent growth. Such a condition was achieved by instantaneous and homogeneous reduction of all the $AuCl_4^-$ precursors by mixing with the strong reducing agent (BH_4^-) in the micromixer. The trend in Figure 1 indicates that

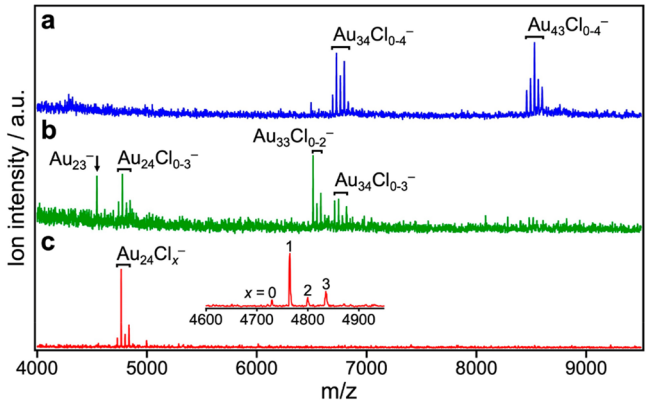

Figure 1. Negative-ion MALDI mass spectra of Au:PVP (**a**–**c**).

PVP also plays an important role in atomically precise synthesis by retarding the nucleation of Au atoms. The ligation by Cl originating from $AuCl_4^-$ has been frequently observed for small Au clusters such as $Au_{34}Cl_n$, $Au_{43}Cl_n$, $[Au_{11}(PPh_3)_8Cl_2]^+$, and $Au_{55}(PPh_3)_{12}Cl_6$.[31,35,36] Elemental analysis of sample **c** determined the average number of the Cl ligands on Au_{24} to be 9.4, suggesting that the MALDI process is accompanied by dissociation of the Cl ligands. Such selective dissociation suggests that the Cl ligands are weakly bound to Au_{24} as electron withdrawing ligands as implied by weak magic behavior at x = 1 and 3 (Figure 1c). Noncontamination of sample **c** with Au NPs larger than 2 nm was confirmed by the following results: (1) absence of the localized surface plasmon resonance (LSPR) band at ∼520 nm in the optical absorption spectrum (Figure 2a); (2) observation of a single broad peak in the powder X-ray

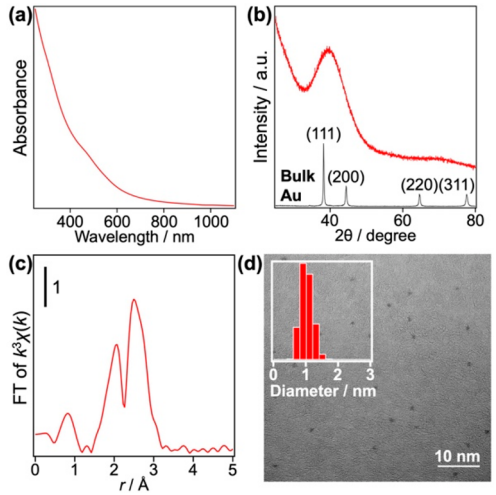

Figure 2. (a) Optical absorption spectrum in water, (b) PXRD pattern, (c) Au L_3-edge FT-EXAFS spectrum, and (d) representative ACTEM image with low magnification of Au:PVP (sample **c**). Results of the curve fitting analysis of Au L_3-edge EXAFS are summarized in Table S1 in the Supporting Information. The inset of panel (d) indicates the diameter distribution of 388 randomly chosen particles.

diffraction (PXRD) pattern (Figure 2b); (3) small coordination number (CN) of the Au–Au bond (4.2 ± 0.5) obtained by the curve-fitting analysis of the Au L_3-edge extended X-ray absorption fine structure (EXAFS) (Figure 2c, Table S1); and (4) mean diameter of the Au clusters estimated to be 1.0 ± 0.2 nm by ACTEM (Figure 2d). We concluded from these results

https://doi.org/10.1021/jacsau.1c00102
JACS Au 2021, 1, 660–668

that single-sized $Au_{24}Cl_x$ was selectively formed in sample **c**. In the following, we focus on sample **c**, which is hereafter referred to as Au_{24}:PVP.

Geometrical Structure of Au_{24}:PVP

It is well-known that the magic stability of naked Au clusters is governed by electronic shell closure based on a jellium model.[37] The formation of Au_{34} and Au_{58} in PVP reported in our previous studies[30,31] is explained by the same model. In contrast, $Au_{24}Cl_x$ in Au_{24}:PVP corresponds to an unprecedented magic cluster. This result implies that the $Au_{24}Cl_x$ cluster does not have a spherical shape and does not provide a spherical potential to confine the valence electrons. To gain insight into the atomic structure of $Au_{24}Cl_x$, we first conducted DFT calculations on Cl-free Au_{24} clusters. Figure 3 lists the DFT-optimized structures of

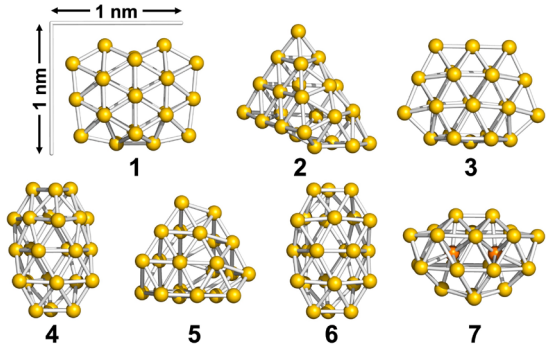

Figure 3. DFT-optimized model structures of Au_{24}.

Au_{24} (**1**−**7**) in the order of the relative stability. The frontier Kohn−Sham orbitals of **1**−**7** are depicted in Figure S1. The relative energies (ΔE) and energy gaps between the highest occupied molecular orbital (HOMO) and the lowest unoccupied molecular orbital (LUMO) are summarized in Table 1. Interestingly, all the constituent Au atoms of structures

Table 1. Relative Energies and HOMO−LUMO Gaps of Model Structures of Au_{24} and $Au_{24}Cl_4$

Au_{24}			$Au_{24}Cl_4$		
model	ΔE/eV[a]	HLG/eV[b]	model	ΔE/eV[a]	HLG/eV[b]
1	0	1.56	**1Cl**	0.33	1.10
2	0.02	1.28	**2Cl**	1.05	1.64
3	0.30	1.12	**3Cl**	0.14	1.64
4	0.31	1.60	**4Cl**	0	1.60
5	0.33	1.11	**5Cl**	0.72	1.25
6	0.61	1.29	**6Cl**	0.18	1.40
7	1.64	1.20	–		

[a]Relative energy. [b]HOMO−LUMO gap.

1−**6** are located on the surface: **1** and **3** have flat cage structures; **4** and **6** have empty tubular shapes; and **2** is constructed by attaching an Au_4 unit to the well-known pyramidal Au_{20} magic cluster.[38] In contrast, the least stable structure **7** contains two Au atoms inside the Au_{22} cage. The dimensions of **1**−**7** fall within the diameter distribution shown in Figure 2d. The projection of **4** or **6** along the longitudinal axis gave the smallest diameter (∼0.7 nm), whereas that of **1** or **3** from the flattened surface normal gave the largest diameter (∼1.3 nm) (Figure S3). This semiquantitative agreement supports the validity of the structural models in Figure 3. These results suggest that various disordered structures such as **1**−**6**, in which all the constituent Au atoms constitute the cluster surface, are energetically accessible. Then, the effect of Cl ligation on the geometrical structures of Au_{24} was studied by using $Au_{24}Cl_4$ with 20 valence electrons as a model. Figure 4 lists the isomeric structures **1Cl**−

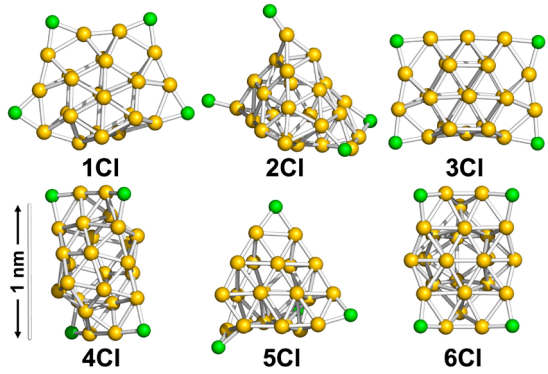

Figure 4. DFT-optimized model structures of $Au_{24}Cl_4$ (Au, yellow; Cl, green).

6Cl obtained by optimizing the initial structures in which four Cl ligands are bonded to low coordination sites of low energy isomers **1**−**6** in Figure 3, respectively. The frontier Kohn−Sham orbitals of **1Cl**−**6Cl** are depicted in Figure S2. Cl ligation induced the slight distortion of the Au frameworks and as a result the relative stability of the isomers was altered. Nevertheless, it is safe to conclude that $Au_{24}Cl_4$ can take isomeric structures in which all the Au atoms are located on the surface, similarly to the naked Au_{24} clusters. The CNs and average lengths of the Au−Au bonds in **1**−**7** and **1Cl**−**6Cl** are summarized in Table S2. The CN values of the Au−Au bonds in **1**−**7** (5.0−5.4) and **1Cl**−**6Cl** (4.2−4.8) qualitatively agreed with that (4.2 ± 0.5) determined by Au L_3-edge EXAFS analysis (Table S1), while the calculated Au−Au bond lengths of **1**−**7** (2.87−2.90 Å) and **1Cl**−**6Cl** (2.85−2.87 Å) are longer than that experimentally determined (2.71 ± 0.01 Å). In the following discussion of the geometrical structures, we ignore the Cl ligands.

Theoretical prediction of energetically comparable isomers suggests that Au_{24} clusters in PVP are composed of distinct structural isomers and/or interconvert among isomers under ambient temperature. To address this interesting issue, atomic structures were probed by ACTEM video imaging at 0.04 s per frame. The ACTEM images of Au_{24}:PVP did not show any signs of atom ejection during continuous observation for several minutes. Figure 5 shows representative ACTEM snapshots of different particles (#1−#4) of Au_{24}:PVP. These images could not be reproduced by considering a single isomeric form in Figure 3 but could be by using different isomers **1**, **2**, **2**, and **5**, respectively. Other snapshots of different particles (#5−#7) in Figure S4 reasonably agree with the images simulated for isomers **4**, **5**, and **7**, respectively. No images could be assigned to the icosahedral nor face-centered cubic structures observed in the selenolate (RSe)- or thiolate (RS)-protected gold clusters $Au_{25}(SeR)_{18}$ and $Au_{144}(SR)_{60}$.[39] Furthermore, the images of a single particle (#8) of Au_{24}:PVP fluctuated every 0.08−0.4 s during the observation period, as exemplified in Figure S5 and Movies S1−S3. Figure 6 shows snapshots of particle #8 taken from the images in Figure S5 at different times (t_1−t_4). Comparison with a set of images simulated by systematically changing the projection directions revealed that the fluctuation of the images was associated with structural isomerization rather than simple rotation of a single isomer: the images of Figure 6a−

https://doi.org/10.1021/jacsau.1c00102
JACS Au 2021, 1, 660−668

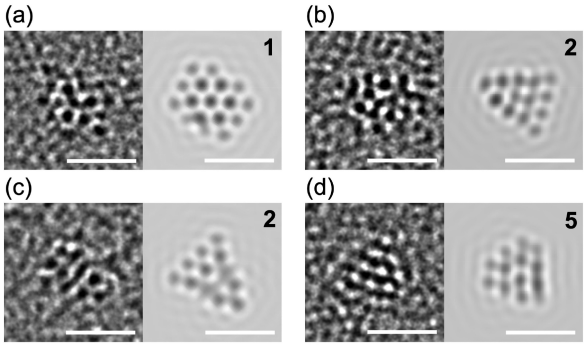

Figure 5. Representative ACTEM snapshots of different particles of Au_{24}:PVP (#1−#4) and simulated TEM images of model structures of Au_{24} in Figure 3. Scale bars correspond to 1 nm.

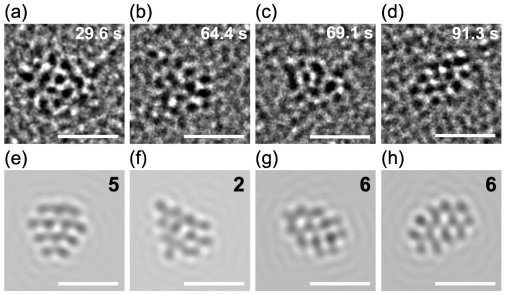

Figure 6. (a−d) Representative ACTEM images of a single particle of Au_{24}:PVP (#8) at different times from the beginning of the video recording (t_1, 29.6 s; t_2, 64.4 s; t_3, 69.1 s; t_4, 91.3 s) and (e−h) simulated images of model structures in Figure 3. Scale bars correspond to 1 nm.

d are assigned to the distinct isomers **5**, **2**, **6**, and **6** (Figure 6e−h), respectively. Thus, we concluded that the individual particles of Au_{24}:PVP interconverted among structural isomers possibly due to migration and/or dissociation of the Cl ligands[40] as well as thermal energy. The coexistence of isomers with hollow tubular structures has also been proposed for the naked cluster anions, Au_{24}^-, in the gas phase.[41] At present, the selective formation of Au_{24}:PVP could not be explained in terms of the electronic nor geometrical shell closure. We speculate that the cavity volume created by the multiple PVP chains determines the preferable and smallest size of Au clusters to be stabilized.

Electronic Structure of Au_{24}:PVP

Although $Au_{24}Cl_x$ was synthesized with atomic precision, the optical absorption spectrum of Au_{24}:PVP in Figure 2a exhibits a featureless profile. This phenomenon was attributed to the coexistence of structural isomers given that the HOMO−LUMO gaps of **1**−**6** varied in the range of 1.1−1.6 eV depending on the atomic structures (Table 1). The electronic structure of Au_{24}:PVP was further characterized by XPS and FT-IR spectroscopy of the adsorbed ^{12}CO with the help of DFT calculations. The XP spectrum of Au_{24}:PVP (Figure 7a) shows an Au $4f_{7/2}$ peak at 82.7 eV, which is red-shifted with respect to that of bulk Au (84.0 eV). This result indicates that $Au_{24}Cl_x$ is negatively charged due to the electron donation from PVP,[24] although DFT calculations showed that the Cl ligands of $Au_{24}Cl_4$ withdrew the electronic charge from Au_{24}: the natural charge of the Cl ligand was ∼−0.5. It is known that the stretching frequency of the adsorbed CO reflects the electron density of the adsorption site on Au clusters.[42−45] FT-IR spectra exhibited a broad peak of ^{12}CO adsorbed on Au_{24}:PVP at 2106 cm^{-1} in addition to that of free ^{12}CO at 2136 cm^{-1} (Figure 7b).

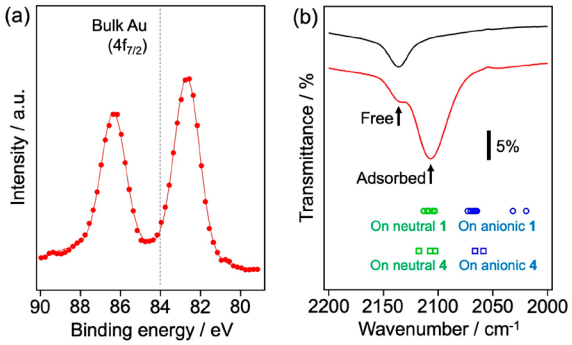

Figure 7. (a) XP spectrum of Au_{24}:PVP. (b) FT-IR spectra of ^{12}CO-saturated dichloromethane (black), ^{12}CO-saturated colloidal dispersion of Au_{24}:PVP (red), and DFT-calculated stretching frequencies of ^{12}CO adsorbed on different adsorption sites of **1** (circle) or **4** (square) with a total charge of 0 (green) or −1 (blue). Details are shown in Tables S3, S4, and Figure S6.

The redshift is ascribed to the π back-donation from the electron-rich Au sites of $Au_{24}Cl_x$.[45] To gain deeper insight into the geometrical and electronic structures of Au_{24}:PVP, CO-adsorbed structures were theoretically studied for two isomers **1** and **4** with charge states of 0 and −1. DFT-optimized structures are illustrated in Figure S6: structural isomers $\mathbf{1COa}^0$−$\mathbf{1COh}^0$ and $\mathbf{1COa}^-$−$\mathbf{1COh}^-$ with different CO adsorption sites were obtained for neutral and anionic **1**, respectively, whereas $\mathbf{4COa}^0$−$\mathbf{4COc}^0$ and $\mathbf{4COa}^-$−$\mathbf{4COc}^-$ were for neutral and anionic **4**, respectively. The adsorption energy and stretching frequency of CO adsorbed on different sites of **1** and **4** are summarized in Tables S3 and S4, respectively. The binding energies are in the range of 0.1−0.4 eV regardless of the structures, charge states, and adsorption sites of Au_{24} clusters. The CO stretching frequencies on neutral **1** and **4** (green plots in Figure 7b) differ only slightly (<20 cm^{-1}) depending on the adsorption sites and can explain the experimental result. On the other hand, the CO stretching frequencies on anionic **1** and **4** (blue plots in Figure 7b) are significantly red-shifted compared to those for neutral **1** and **4**. Although these results could not identify the structure of the $Au_{24}Cl_x$ core and adsorption site of CO, they imply that the negative charge on the $Au_{24}Cl_x$ core is smaller than 1e as a result of a balance between the electron-withdrawing nature of Cl and the electron-donating nature of PVP.

Aerobic Oxidation Catalysis of Au_{24}:PVP

Since Haruta's discovery of CO oxidation catalyzed by Au NPs on metal oxide supports,[46] the catalytic properties of nanosized Au have attracted considerable interest in nanoscience.[47−50] In particular, alcohol oxidation is catalyzed efficiently by Au-based catalysts[5,51,52] and has been studied as a model reaction to investigate the effects of structural parameters on the catalysis. For example, we have demonstrated that Au:PVP shows size-specific and high catalytic activities for aerobic alcohol oxidation.[22,24] However, these studies were conducted using monodisperse Au clusters but with distributions in the number of constituent atoms. Au_{24}:PVP synthesized here provides a novel opportunity to study atomistic details of the catalytic mechanism.

Kinetic measurements were conducted for the aerobic oxidation of *p*-substituted benzyl alcohol X-$C_6H_4CH_2OH$ (X = OCH_3, CH_3, H, CF_3) catalyzed by Au_{24}:PVP (Figure 8a). The selectivity of products between the aldehydes and carboxylic

https://doi.org/10.1021/jacsau.1c00102
JACS Au 2021, 1, 660−668

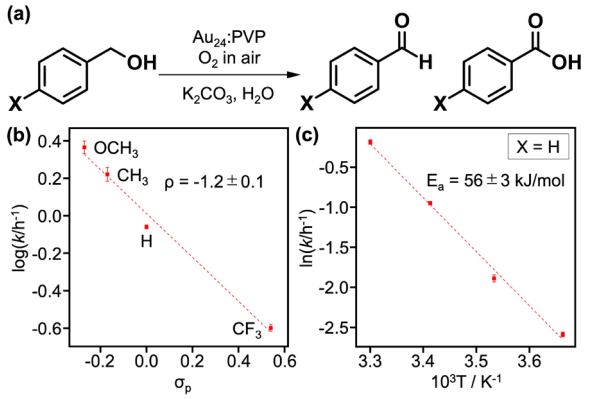

Figure 8. (a) Aerobic oxidation of *p*-substituted benzyl alcohol X–$C_6H_4CH_2OH$ (X = OCH_3, CH_3, H, CF_3) catalyzed by Au_{24}:PVP. (b) Hammett plot for the aerobic oxidation of *p*-substituted benzyl alcohol catalyzed by Au_{24}:PVP dispersed in H_2O.[53] (c) Arrhenius plot for the benzyl alcohol oxidation (X = H). Reaction conditions: substrate 80 μmol; Au_{24}:PVP 5 atom %; K_2CO_3 300 mol %; H_2O 20 mL; air; 303 K (unless specified).

acids depended on the substituent group X (Figure S7). The pseudo-first-order rate constant was determined from the time course of the alcohol concentration (Figure S8). The effect of X on the rate constant was analyzed using the Hammett plot (Figure 8b). The negative reaction constant ($\rho = -1.2 \pm 0.2$) indicates that the benzylic carbon has cationic characteristics at the transition state of the rate-limiting step. Furthermore, a large KIE ($k_H/k_D = 4.1$) was observed for α-deuterated benzyl alcohol ($C_6H_5CD_2OH$). Thus, it was concluded that the C–H bond cleavage at the benzylic position was the rate-limiting step and that the H atom was abstracted as a hydride. The apparent activation energy for X = H was estimated to be 56 ± 3 kJ/mol from the Arrhenius plot (Figure 8c).

Importantly, MALDI-MS, optical spectroscopy, and Au L_3-edge EXAFS confirmed that the cluster size of Au_{24}:PVP was retained during the catalytic reactions under the present conditions (Figures S9–S19). In contrast, MALDI-MS and Au L_3-edge EXAFS suggested the loss of Cl ligands during the reaction (Figures S9–S19). These results indicate that the catalysis is governed by Au_{24} and not affected by the Cl ligands. The negligible effect of the Cl ligands on the catalysis was supported by the fact that different batches of Au_{24}:PVP having a different number of Cl ligands showed a similar activity (Figures S9 and S15). It was also reported that the Cl ligands of PVP-stabilized $Au_{34}Cl_n$ and $Au_{43}Cl_n$ were easily released during the reactions and did not prevent the catalytic alcohol oxidation.[31]

Two different mechanisms have been proposed for aerobic alcohol oxidation in which O_2 plays different roles. We have proposed that O_2 is reductively activated upon adsorption onto the negatively charged Au:PVP based on the correlation between the electron affinities of naked Au_n and the reactivity to O_2.[24] In this mechanism, the resulting superoxo-like species abstracts hydrogen from the α-carbon of coadsorbed alkoxide (Scheme 1a).[25] A similar mechanism has been proposed by Ebitani in the alcohol oxidation by hydrotalcite-supported metal (AuPd, AuPt or Pt) NPs costabilized by polymers such as PVP and starch.[54−56] The other mechanism, proposed by Kobayashi, Chechik, and co-workers is based on the observation of an Au–H intermediate during the alcohol oxidation on Au NPs stabilized by styrene-based copolymers (Au:PS): hydride is directly transferred to the Au NP surface (Scheme 1b) and

Scheme 1. Previously Proposed Reaction Mechanisms of Alcohol Oxidation Catalyzed by (a) Au:PVP and (b) Au:PS

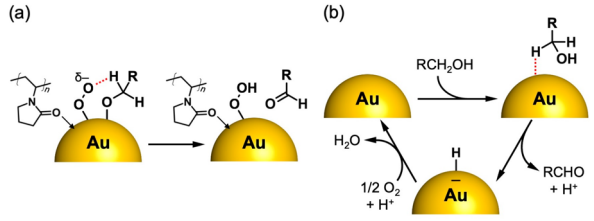

adsorbed hydrogen is removed by O_2.[57] This hydride elimination mechanism has been accepted for alcohol oxidation by Au NPs supported on metal oxides such as TiO_2, CeO_2, and Al_2O_3.[58−63] A similar reaction mechanism has been proposed by Kaneda for alcohol oxidation catalyzed by hydroxyapatite-supported Pd clusters.[64]

The reaction constant for Au_{24}:PVP determined by the Hammett plot under air (Figure 8b, -1.2 ± 0.2) is comparable to those reported for Au NPs supported on metal oxides (-0.2 to -1.4).[58,59,61,63] This fact also lends support for the hydride elimination mechanism by Au_{24} (Scheme 1b). To gain further insight into the mechanism by Au_{24}:PVP, the effect of O_2 pressure was investigated. The time course of the alcohol oxidation under 1 atm of O_2 (Figure 9a) showed two

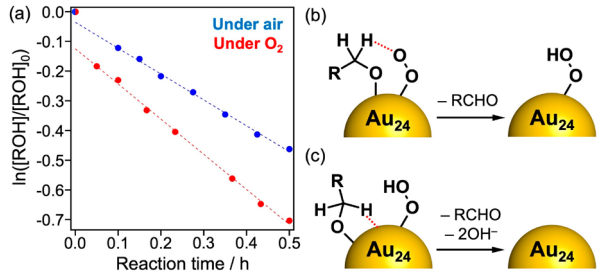

Figure 9. (a) Natural logarithm of benzyl alcohol concentration (normalized by initial concentration) during the catalytic oxidation reaction under air (blue, O_2: 0.21 atm) or pure O_2 (red, O_2: 1 atm). Conditions other than O_2 pressure were the same as those for Figure 8. Two alcohol oxidation pathways on Au_{24}:PVP: (b) hydrogen abstraction by O_2 and (c) hydride elimination by Au_{24}.

characteristic behaviors: (1) for $t > 0.05$ h, the rate constant under pure O_2 (1.18 h^{-1}) was larger than that under air (O_2: 0.21 atm, 0.87 h^{-1}), although the rate constants were not proportional to the oxygen pressure; (2) the rate constant at the initial stage ($t < 0.05$ h) was apparently larger than that for $t > 0.05$ h. The former can be explained by the hydride elimination mechanism (Scheme 1b) with the assumption that the catalyst recovery by O_2 is not much faster than the hydride elimination. However, it was difficult to rationalize the latter only by hydride elimination mechanism. We propose that hydrogen abstraction by O_2 (Figure 9b) is involved in addition to the rate-limiting hydride elimination by Au_{24} (Figure 9c). Involvement of the two mechanisms was supported by a recent theoretical study on the oxidation of *p*-hydroxybenzyl alcohol by a model cluster $Au_{38}L_3$ (L = 2-pyrrolidone) reported by Okumura et al.[65] It was concluded that the most energetically plausible catalytic cycle is composed of two consecutive steps: hydrogen abstraction by O_2 (step 1) and hydride elimination by Au_{38} (step 2):

https://doi.org/10.1021/jacsau.1c00102
JACS Au 2021, 1, 660–668

Step 1: $ArCH_2O^- + O_2 + [Au_{38}L_3] \rightarrow ArCHO + [(HOO)Au_{38}L_3]^-$
Step 2: $ArCH_2O^- + [(HOO)Au_{38}L_3]^- \rightarrow ArCHO + 2OH^- + [Au_{38}L_3]$

The cooperation of two oxidation steps was ascribed to the order of the reactivities of oxidants: (O_2 on Au_{38}) > (Au_{38} surface) > (HOO on Au_{38}).

CONCLUSION

In summary, a novel magic number cluster, Au_{24}:PVP, was serendipitously and reproducibly obtained by homogenizing the formation process using a micromixer and limiting the growth step by the presence of a large amount of PVP. ACTEM video imaging revealed the polydispersity and fluxionality of the atomic structure of Au_{24}:PVP. Noncrystalline structures with all constituent Au atoms on the surface are suggested by DFT calculations. We speculate that the observation of an unprecedented magic number is associated with the cavity size created by assemblies of PVP in which Au clusters can be confined. Au_{24}:PVP catalyzed the aerobic oxidation of benzyl alcohol derivatives while retaining the size. Kinetics studies revealed that the hydride elimination from benzylic carbon by Au_{24} corresponds to the rate-limiting step with an apparent activation energy of 56 ± 3 kJ/mol. It was also suggested from the O_2 pressure dependence on the reaction kinetics that the hydrogen abstraction by the adsorbed O_2 is involved as well. We propose that the oxidation is initiated by the hydrogen abstraction by O_2 adsorbed on Au_{24}, followed by the rate-limiting hydride elimination by Au_{24}.

METHODS

Chemicals

All chemicals were commercially available and were used without further purification. Hydrogen tetrachloroaurate(III) tetrahydrate, sodium borohydride, PVP (K30, average molecular weight: ~40 000), benzyl alcohol, *p*-methylbenzyl alcohol, *p*-methoxybenzyl alcohol, and potassium carbonate were purchased from Wako Pure Chemical Industries. *trans*-2-[3-(4-*tert*-Butylphenyl)-2-methyl-2-propenylidene]malononitrile (DCTB) and *p*-(trifluoromethyl)benzyl alcohol were purchased from Tokyo Chemical Industry. Deuterated benzyl alcohol ($C_6H_5CD_2OH$) was purchased from Sigma-Aldrich. Deionized water used was Milli-Q grade (>18 MΩ cm).

Synthesis

Au clusters were synthesized by microfluidic mixing of two aqueous solutions of Au precursors and a reducing agent as reported previously.[29−31] The ice-cooled aqueous solution of $HAuCl_4$ and PVP was mixed with that of $NaBH_4$ and PVP at a flow rate of 200 mL/h in a micromixer (SIMM-V2, IMM GmbH) placed in an ice bath. Three samples of Au:PVP (**a**−**c**) were obtained by tuning the [Au]:[PVP] mixing ratios as listed in Table 2. The resulting brown solution was collected in an Erlenmeyer flask, stirred for 1 h at 273 K, and then deionized four times at 273 K by using a centrifugal ultrafiltration concentrator (Vivaspin20, Vivascience) having a membrane filter with a cutoff molecular weight of 10 kDa (for **a**) or 100 kDa (for **b** and **c**). The deionized solution was lyophilized to obtain Au:PVP in a powder form. The yields of **a**−**c** were 79, 73, and 79%, respectively, based on the amount of Au. Optical absorption spectroscopy and thermogravimetry showed that the amount of PVP was reduced to ~40 equiv (monomer unit to Au atom) by ultrafiltration. PVP was added to adjust the equivalence to 50 in the catalytic tests.

Table 2. Conditions of Synthesizing Au:PVP

	Au precursor		reducing agent		
sample	[$HAuCl_4$]/mM	[PVP]/mM[a]	[$NaBH_4$]/mM	[PVP]/mM[a]	[Au]:[$NaBH_4$]:[PVP][a]
a	10	200	50	200	1:5:40
b	10	500	50	500	1:5:100
c	10	1000	50	1000	1:5:200

[a]Concentrations of monomer unit.

Characterization

MALDI mass spectra were recorded using a time-of-flight mass spectrometer (AXIMA-CFR, Shimadzu): DCTB was used as a matrix. The specimens for MALDI-MS were prepared by drop-casting a methanol dispersion of Au:PVP and DCTB ([Au]:[DCTB] = 1:18) onto a sample plate. Optical absorption spectra were recorded by using a spectrophotometer (V-670, JASCO). The PXRD pattern was obtained using a diffractometer with CuKα radiation (SmartLab 3, Rigaku). ACTEM was carried out on a JEM-ARM200F instrument (JEOL) at an acceleration voltage of 80 kV, under 1×10^{-5} Pa at 298 K in the specimen column. A series of ACTEM images were continuously recorded at 25 frames per second (fps) on a CMOS camera (Gatan OneView with in situ option, output image size: 2,048 × 2,048 pixels operated in the binning 2 mode, pixel resolution: 0.01 nm at ×2 000 000 magnification). We adjusted the spherical aberration value, electron dose rate, and defocus value to 1−3 μm, 2.7−5.6 × 10^6 e^- nm^{-2} s^{-1}, approximately −4 nm (underfocus), respectively. Acquired images were filtered by a bandpass filter using ImageJ software;[66] structures larger than 40 pixels or smaller than 3 pixels were filtered with the tolerance of direction of 5%. The specimens for ACTEM were prepared by drop-casting a methanol dispersion of Au:PVP onto a thin carbon-coated copper grid (SHR-C075, Okenshoji). The average diameter was determined by measuring the diameters of 388 particles in low magnification (×800 000) images. XPS was carried out using a PHI-5000 VersaProbe (ULVAC-PHI) instrument at an energy resolution of 0.2 eV. Electron binding energy was calibrated referring to the Au $4f_{7/2}$ peak of bulk Au (84.0 eV). FT-IR spectra of carbon monoxide adsorbed on Au:PVP were measured by using a spectrophotometer (FTIR-4200, Jasco) in the transmission mode at a resolution of 2 cm^{-1}. For FT-IR measurements, Au:PVP (Au 15 μmol) was dispersed in dichloromethane (3 mL) under CO (1.0 atm) and the colloidal dispersion was introduced into the IR cell (CaF_2 window, 0.5 mm path length) after the stirring for 50 min. Au L_3-edge X-ray absorption spectroscopy (XAS) was conducted in the transmission mode using the BL01B1 beamline at SPring-8 of the Japan Synchrotron Radiation Research Institute (JASRI). The incident X-ray beam was monochromatized by a Si (111) double crystal monochromator. The spectral data were analyzed by using the REX2000 program (Rigaku). The k^3-weighted χ spectra in the k range of 3−16.5 $Å^{-1}$ were Fourier-transformed into the r space. The Au−Au and Au−Cl bonds were considered in the curve-fitting analysis over the r range of 1.7−3.0 Å.

Calculations and Simulations

DFT calculations of the model structures of Au_{24}, $Au_{24}Cl_4$, and $Au_{24}(CO)_1$ were performed using the Gaussian 09 program.[67] B3LYP was used as a functional.[68,69] A double-ζ basis set with scalar relativistic effective core potential (ECP), LANL2DZ, was applied for Au and the 6-31+G(d) basis set was used for C, O, and Cl. Structures of Au_{24} were obtained by reoptimization of those reported previously.[70,71] PVP was not included in the calculations since the impact on the atomic structure of Au clusters is negligibly small.[72] Neutral clusters (Au_{24}, $Au_{24}(CO)_1$, and $Au_{24}Cl_4$) were optimized with the singlet spin state, whereas the doublet spin state was applied for the anionic cluster, $Au_{24}(CO)_1^-$. The vibrational frequencies were computed for the optimized structures to ensure that they corresponded to the local minima of the potential energy surface. The relative energy of the clusters presented in this study includes the zero-point energy. For the stretching frequencies of CO adsorbed on Au_{24}, a scaling factor of 0.970 was applied so that the calculated frequency of isolated CO (2203 cm^{-1}) reproduced that of free CO in dichloromethane (2136 cm^{-1}).

TEM simulation images of DFT-optimized structures were generated by using a multislice procedure implemented in a BioNet

https://doi.org/10.1021/jacsau.1c00102
JACS Au 2021, 1, 660−668

elbis software:[73] DFT-optimized structures were converted to a series of simulated TEM images with the observation direction varying every 10° around the x and y axes, producing 18 × 36 = 648 images.[74] A defocus value of −4 nm and a spherical aberration coefficient (Cs) of −3 μm were applied for the simulation. To quantify the similarity of the experimental and simulated images, a cross-correlation analysis was conducted.[75,76] The cross-correlation function of two images (a and b), $\gamma(a, b)$, is defined as follows:

$$\gamma(a, b) = \frac{\sum_{i,j}^{N} [I_a(r_{i,j}) - \overline{I}_a] \cdot [I_b(r_{i,j}) - \overline{I}_b]}{\sqrt{\sum_{i,j}^{N} [\mathrm{dI}_a(r_{i,j}) - \overline{I}_a]^2} \cdot \sqrt{\sum_{i,j}^{N} [I_b(r_{i,j}) - \overline{I}_b]^2}}$$

where I, $r_{i,j}$, and $\overline{I}$ represent the intensity of the image, pixel position, and mean intensity, respectively. The value of this function is an index of the similarity of images; γ of 1 or 0 corresponds to a perfect match or no match, respectively. Therefore, the cross-correlation function of the experimental and simulated images was calculated for the efficient screening of the large number of simulated images. Candidate images obtained by the screening were then carefully compared to the experimental images.

Catalytic Test

Catalytic properties of Au:PVP for aerobic oxidation of benzyl alcohol derivatives in water were studied by using a temperature-controlled personal organic synthesizer, PPS-2510 (Eyela). The catalytic reaction was initiated by adding the aqueous dispersion (8 mL) of Au:PVP (4 μmol) to the aqueous solution (12 mL) of alcohol (80 μmol) and K_2CO_3 (240 μmol) magnetically stirred at 800 rpm. Aliquots (5 mL) were sampled at the given time and hydrochloric acid (HCl 600 μmol in 150 μL) was added to quench the reaction. Reaction products were extracted by ethyl acetate (1 mL) three times. The extract thus collected was dried over Na_2SO_4 and analyzed by a gas chromatograph (GC-2014, Shimadzu) with a flame ionization detector. Rate constants for the oxidation reaction were obtained by linear fitting of the natural logarithm of the alcohol concentration using ≥7 data points at which the conversion was typically between 10% and 40%. Since the reaction proceeds faster in the initial stage (conv. < 10%), the zero point was excluded for the linear fitting.

■ ASSOCIATED CONTENT

Supporting Information

The Supporting Information is available free of charge at https://pubs.acs.org/doi/10.1021/jacsau.1c00102.

Supplementary tables and figures for Au L_3-edge XAS, DFT calculations, ACTEM, and catalytic tests (PDF)

Movie S1: ACTEM video of a single particle (#8) of Au_{24}:PVP at 24.04−36.00 s (AVI)

Movie S2: ACTEM video of a single particle (#8) of Au_{24}:PVP at 60.04−72.00 s (AVI)

Movie S3: ACTEM video of a single particle (#8) of Au_{24}:PVP at 84.04−96.00 s (AVI)

■ AUTHOR INFORMATION

Corresponding Author

Tatsuya Tsukuda − *Department of Chemistry, Graduate School of Science, The University of Tokyo, Tokyo 113-0033, Japan; Elements Strategy Initiative for Catalysts and Batteries (ESICB), Kyoto University, Kyoto 615-8520, Japan;* orcid.org/0000-0002-0190-6379; Email: tsukuda@chem.s.u-tokyo.ac.jp

Authors

Shingo Hasegawa − *Department of Chemistry, Graduate School of Science, The University of Tokyo, Tokyo 113-0033, Japan*

Shinjiro Takano − *Department of Chemistry, Graduate School of Science, The University of Tokyo, Tokyo 113-0033, Japan;* orcid.org/0000-0001-9262-5283

Koji Harano − *Department of Chemistry, Graduate School of Science, The University of Tokyo, Tokyo 113-0033, Japan;* orcid.org/0000-0001-6800-8023

Complete contact information is available at: https://pubs.acs.org/10.1021/jacsau.1c00102

Notes

The authors declare no competing financial interest.

■ ACKNOWLEDGMENTS

The authors thank Mr. Ko Kamei (The University of Tokyo) for supporting TEM simulation. This research was financially supported by JST CREST Grant Number JPMJCR20B2, the Elements Strategy Initiative for Catalysts & Batteries (ESICB) (Grant No. JPMXP0112101003) and the Nanotechnology Platform (Project No. 12024046) of MEXT, a Grant-in-Aid for Scientific Research (A) (No. 20H00370), and a JSPS Research Fellow Grant (No. JP19J22154) from JSPS. The synchrotron radiation experiments were performed under the approval of JASRI (Proposal No. 2020A0672). Calculations were partly performed using the Research Center for Computational Science, Okazaki, Japan.

■ REFERENCES

(1) Yamazoe, S.; Koyasu, K.; Tsukuda, T. Nonscalable Oxidation Catalysis of Gold Clusters. *Acc. Chem. Res.* **2014**, *47*, 816−824.

(2) Jin, R.; Zeng, C.; Zhou, M.; Chen, Y. Atomically Precise Colloidal Metal Nanoclusters and Nanoparticles: Fundamentals and Opportunities. *Chem. Rev.* **2016**, *116*, 10346−10413.

(3) Chakraborty, I.; Pradeep, T. Atomically Precise Clusters of Noble Metals: Emerging Link between Atoms and Nanoparticles. *Chem. Rev.* **2017**, *117*, 8208−8271.

(4) Ye, R.; Zhukhovitskiy, A. V.; Deraedt, C. V.; Toste, F. D.; Somorjai, G. A. Supported Dendrimer-Encapsulated Metal Clusters: Toward Heterogenizing Homogeneous Catalysts. *Acc. Chem. Res.* **2017**, *50*, 1894−1901.

(5) Liu, L.; Corma, A. Metal Catalysts for Heterogeneous Catalysis: From Single Atoms to Nanoclusters and Nanoparticles. *Chem. Rev.* **2018**, *118*, 4981−5079.

(6) Du, Y.; Sheng, H.; Astruc, D.; Zhu, M. Atomically Precise Noble Metal Nanoclusters as an Efficient Catalysts: A Bridge between Structure and Properties. *Chem. Rev.* **2020**, *120*, 526−622.

(7) Li, Z.; Ji, S.; Liu, Y.; Cao, X.; Tian, S.; Chen, Y.; Niu, Z.; Li, Y. Well-Defined Materials for Heterogeneous Catalysis: From Nanoparticles to Isolated Single-Atom Sites. *Chem. Rev.* **2020**, *120*, 623−682.

(8) Yamamoto, K.; Imaoka, T.; Tanabe, M.; Kambe, T. New Horizon of Nanoparticle and Cluster Catalysis with Dendrimers. *Chem. Rev.* **2020**, *120*, 1397−1437.

(9) Kawawaki, T.; Negishi, Y.; Kawasaki, H. Photo/Electrocatalysis and Photosensitization Using Metal Nanoclusters for Green Energy and Medical Applications. *Nanoscale Adv.* **2020**, *2*, 17−36.

(10) Jin, R.; Li, G.; Sharma, S.; Li, Y.; Du, X. Toward Active-Site Tailoring in Heterogeneous Catalysis by Atomically Precise Metal Nanoclusters with Crystallographic Structures. *Chem. Rev.* **2021**, *121*, 567−648.

(11) Omoda, T.; Takano, S.; Tsukuda, T. Toward Controlling the Electronic Structures of Chemically Modified Superatoms of Gold and Silver. *Small* **2020**, 2001439.

(12) Wang, Y.; Wan, X.-K.; Ren, L.; Su, H.; Li, G.; Malola, S.; Lin, S.; Tang, Z.; Häkkinen, H.; Teo, B. K.; Wang, Q. M.; Zheng, N. Atomically Precise Alkynyl-Protected Metal Nanoclusters as a Model Catalyst:

Observation of Promoting Effect of Surface Ligands on Catalysis by Metal Nanoparticles. *J. Am. Chem. Soc.* **2016**, *138*, 3278−3281.
(13) Narayanan, R.; El-Sayed, M. A. Effect of Catalysis on the Stability of Metallic Nanoparticles: Suzuki Reaction Catalyzed by PVP-Palladium Nanoparticles. *J. Am. Chem. Soc.* **2003**, *125*, 8340−8347.
(14) Grass, M. E.; Zhang, W.; Butcher, D. R.; Park, J. Y.; Li, Y.; Bluhm, H.; Bratlie, K. M.; Zhang, T.; Somorjai, G. A. A Reactive Oxide Overlayer on Rhodium Nanoparticles during CO Oxidation and Its Size Dependence Studied by in situ Ambient-Pressure X-ray Photoelectron Spectroscopy. *Angew. Chem., Int. Ed.* **2008**, *47*, 8893−8896.
(15) Santiago González, B.; Rodríguez, M. J.; Blanco, C.; Rivas, J.; López-Quintela, M. A.; Martinho, J. M. G. One Step Synthesis of the Smallest Photoluminescent and Paramagnetic PVP-Protected Gold Atomic Clusters. *Nano Lett.* **2010**, *10*, 4217−4421.
(16) Balcha, T.; Strobl, J. R.; Fowler, C.; Dash, P.; Scott, R. W. J. Selective Aerobic Oxidation of Crotyl Alcohol Using AuPd Core-Shell Nanoparticles. *ACS Catal.* **2011**, *1*, 425−436.
(17) Zhang, H.; Watanabe, T.; Okumura, M.; Haruta, M.; Toshima, N. Catalytically Highly Active Top Gold Atom on Palladium Nanocluster. *Nat. Mater.* **2012**, *11*, 49−52.
(18) Yuan, Y.; Yan, N.; Dyson, P. J. Advances in the Rational Design of Rhodium Nanoparticle Catalysts: Control via Manipulation of the Nanoparticle Core and Stabilizer. *ACS Catal.* **2012**, *2*, 1057−1069.
(19) Kusada, K.; Kitagawa, H. A Route for Phase Control in Metal Nanoparticles: A Potential Strategy to Create Advanced Materials. *Adv. Mater.* **2016**, *28*, 1129−1142.
(20) Axet, M. R.; Philippot, K. Catalysis with Colloidal Ruthenium Nanoparticles. *Chem. Rev.* **2020**, *120*, 1085−1145.
(21) Hasegawa, S.; Tsukuda, T. Exploring Novel Catalysis Using Polymer-Stabilized Metal Clusters. *Bull. Chem. Soc. Jpn.* **2021**, *94*, 1036−1044.
(22) Tsunoyama, H.; Sakurai, H.; Negishi, Y.; Tsukuda, T. Size-Specific Catalytic Activity of Polymer-Stabilized Gold Nanoclusters for Aerobic Alcohol Oxidation in Water. *J. Am. Chem. Soc.* **2005**, *127*, 9374−9375.
(23) Sakurai, H.; Tsunoyama, H.; Tsukuda, T. Oxidative Homo-Coupling of Potassium Aryltrifluoroborates Catalyzed by Gold Nanocluster under Aerobic Conditions. *J. Organomet. Chem.* **2007**, *692*, 368−374.
(24) Tsunoyama, H.; Ichikuni, N.; Sakurai, H.; Tsukuda, T. Effect of Electronic Structures of Au Clusters Stabilized by Poly(*N*-vinyl-2-pyrrolidone) on Aerobic Oxidation Catalysis. *J. Am. Chem. Soc.* **2009**, *131*, 7086−7093.
(25) Tsukuda, T.; Tsunoyama, H.; Sakurai, H. Aerobic Oxidations Catalyzed by Colloidal Nanogold. *Chem. - Asian J.* **2011**, *6*, 736−748.
(26) Haesuwannakij, S.; Kimura, T.; Furutani, Y.; Okumura, K.; Kokubo, K.; Sakata, T.; Yasuda, H.; Yakiyama, Y.; Sakurai, H. The Impact of the Polymer Chain Length on the Catalytic Activity of Poly(*N*-vinyl-2-pyrrolidone)-Supported Gold Nanoclusters. *Sci. Rep.* **2017**, *7*, 9579.
(27) Tsunoyama, H.; Sakurai, H.; Tsukuda, T. Size Effect on the Catalysis of Gold Clusters Dispersed in Water for Aerobic Oxidation of Alcohol. *Chem. Phys. Lett.* **2006**, *429*, 528−532.
(28) Niihori, Y.; Yoshida, K.; Hossain, S.; Kurashige, W.; Negishi, Y. Deepening the Understanding of Thiolate-Protected Metal Clusters Using High-Performance Liquid Chromatography. *Bull. Chem. Soc. Jpn.* **2019**, *92*, 664−695.
(29) Tsunoyama, H.; Ichikuni, N.; Tsukuda, T. Microfluidic Synthesis and Catalytic Application of PVP-Stabilized ∼ 1 nm Gold Clusters. *Langmuir* **2008**, *24*, 11327−11330.
(30) Tsunoyama, H.; Tsukuda, T. Magic Numbers of Gold Clusters Stabilized by PVP. *J. Am. Chem. Soc.* **2009**, *131*, 18216−18217.
(31) Ishida, R.; Arii, S.; Kurashige, W.; Yamazoe, S.; Koyasu, K.; Negishi, Y.; Tsukuda, T. Halogen Adsorbates on Polymer-Stabilized Gold Clusters: Mass Spectrometric Detection and Effects on Catalysis. *Chin. J. Catal.* **2016**, *37*, 1656−1661.
(32) Bals, S.; Van Aert, S.; Romero, C.P.; Lauwaet, K.; Van Bael, M.J.; Schoeters, B.; Partoens, B.; Yucelen, E.; Lievens, P.; Van Tendeloo, G. Atomic Scale Dynamics of Ultrasmall Germanium Clusters. *Nat. Commun.* **2012**, *3*, 897.
(33) Lambie, S. G.; Weal, G. R.; Blackmore, C. E.; Palmer, R. E.; Garden, A. L. Contrasting Motif Preferences of Platinum and Gold Nanoclusters between 55 and 309 atoms. *Nanoscale Adv.* **2019**, *1*, 2416−2425.
(34) La Mer, V. K. Nucleation in Phase Transitions. *Ind. Eng. Chem.* **1952**, *44*, 1270−1277.
(35) Schmid, G. The Relevance of Shape and Size of Au_{55} Clusters. *Chem. Soc. Rev.* **2008**, *37*, 1909−1930.
(36) McKenzie, L. C.; Zaikova, T. O.; Hutchison, J. E. Structurally Similar Triphenylphosphine-Stabilized Undecagolds, $Au_{11}(PPh_3)_7Cl_3$ and $[Au_{11}(PPh_3)_8Cl_2]Cl$, Exhibit Distinct Ligand Exchange Pathways with Glutathione. *J. Am. Chem. Soc.* **2014**, *136*, 13426−13435.
(37) de Heer, W. A. The Physics of Simple Metal Clusters: Experimental Aspects and Simple Models. *Rev. Mod. Phys.* **1993**, *65*, 611−676.
(38) Li, J.; Li, X.; Zhai, H.-J.; Wang, L. S. Au_{20}: A Tetrahedral Cluster. *Science* **2003**, *299*, 864−867.
(39) Takahata, R.; Yamazoe, S.; Maehara, Y.; Yamazaki, K.; Takano, S.; Kurashige, W.; Negishi, Y.; Gohara, K.; Tsukuda, T. Electron Microscopic Observation of an Icosahedral Au_{13} Core in $Au_{25}(SePh)_{18}$ and Reversible Isomerization between Icosahedral and Face-Centered Cubic Cores in $Au_{144}(SC_2H_4Ph)_{60}$. *J. Phys. Chem. C* **2020**, *124*, 6907−6912.
(40) Kang, X.; Zhu, M. Structural Isomerism in Atomically Precise Nanoclusters. *Chem. Mater.* **2021**, *33*, 39−62.
(41) Khetrapal, N. S.; Bulusu, S. S.; Zeng, X. C. Structural Evolution of Gold Clusters Au_n^- (n = 21−25) Revisited. *J. Phys. Chem. A* **2017**, *121*, 2466−2474.
(42) Yoon, B.; Häkkinen, H.; Landman, U.; Wörz, A. S.; Antonietti, J.-M.; Abbet, S.; Judai, K.; Heiz, U. Charging Effects on Bonding and Catalyzed Oxidation of CO on Au_8 Clusters on MgO. *Science* **2005**, *307*, 403−407.
(43) Sterrer, M.; Yulikov, M.; Fischbach, E.; Heyde, M.; Rust, H.-P.; Pacchioni, G.; Risse, T.; Freund, H.-J. Interaction of Gold Clusters with Color Centers on MgO(001) Films. *Angew. Chem., Int. Ed.* **2006**, *45*, 2630−2632.
(44) Fielicke, A.; von Helden, G.; Meijer, G.; Pedersen, D. B.; Simard, B.; Rayner, D. M. Gold Cluster Carbonyls: Saturated Adsorption of CO on Gold Cluster Cations, Vibrational Spectroscopy, and Implications for Their Structures. *J. Am. Chem. Soc.* **2005**, *127*, 8416−8423.
(45) Chen, M.; Goodman, D. W. Catalytically Active Gold: From Nanoparticles to Ultrathin Films. *Acc. Chem. Res.* **2006**, *39*, 739−746.
(46) Haruta, M.; Kobayashi, T.; Sano, H.; Yamada, N. Novel Gold Catalysts for the Oxidation of Carbon Monoxide at a Temperature Far Below 0 °C. *Chem. Lett.* **1987**, *16*, 405−408.
(47) Mitsudome, T.; Kaneda, K. Gold Nanoparticle Catalysts for Selective Hydrogenation. *Green Chem.* **2013**, *15*, 2636−2654.
(48) Takale, B. S.; Bao, M.; Yamamoto, Y. Gold Nanoparticle (AuNPs) and Gold Nanopore (AuNPore) Catalysts in Organic Synthesis. *Org. Biomol. Chem.* **2014**, *12*, 2005−2027.
(49) Ishida, T.; Murayama, T.; Taketoshi, A.; Haruta, M. Importance of Size and Contact Structure of Gold Nanoparticles for the Genesis of Unique Catalytic Processes. *Chem. Rev.* **2020**, *120*, 464−525.
(50) Sankar, M.; He, Q.; Engel, R. V.; Sainna, M. A.; Logsdail, A. J.; Roldan, A.; Willock, D. J.; Agarwal, N.; Kiely, C. J.; Hutchings, G. J. Role of the Support in Gold-Containing Nanoparticles as Heterogeneous Catalysts. *Chem. Rev.* **2020**, *120*, 3890−3938.
(51) Abad, A.; Concepción, P.; Corma, A.; García, H. A Collaborative Effect between Gold and a Support Induces the Selective Oxidation of Alcohols. *Angew. Chem., Int. Ed.* **2005**, *44*, 4066−4069.
(52) Enache, D. I.; Edwards, J. K.; Landon, P.; Solsona-Espriu, B.; Carley, A. F.; Herzing, A. A.; Watanabe, M.; Kiely, C. J.; Knight, D. W.; Hutchings, G. J. Solvent-Free Oxidation of Primary Alcohols to Aldehydes Using Au-Pd/TiO_2 Catalysts. *Science* **2006**, *311*, 362−365.
(53) Hansch, C.; Leo, A.; Taft, R. W. A Survey of Hammett Substituent Constants and Resonance and Field Parameters. *Chem. Rev.* **1991**, *91*, 165−195.

https://doi.org/10.1021/jacsau.1c00102
JACS Au 2021, 1, 660−668

(54) Nishimura, S.; Yakita, Y.; Katayama, M.; Higashimine, K.; Ebitani, K. The Role of Negatively Charged Au States in Aerobic Oxidation of Alcohols over Hydrotalcite Supported AuPd Nanoclusters. *Catal. Sci. Technol.* **2013**, *3*, 351−359.
(55) Tongsakul, D.; Nishimura, S.; Ebitani, K. Platinum/Gold Alloy Nanoparticles-Supported Hydrotalcite Catalyst for Selective Aerobic Oxidation of Polyols in Base-Free Aqueous Solution at Room Temperature. *ACS Catal.* **2013**, *3*, 2199−2207.
(56) Tongsakul, D.; Nishimura, S.; Ebitani, K. Effect of Stabilizing Polymers on Catalysis of Hydrotalcite-Supported Platinum Nanoparticles for Aerobic Oxidation of 1,2-Propanediol in Aqueous Solution at Room Temperature. *J. Phys. Chem. C* **2014**, *118*, 11723−11730.
(57) Conte, M.; Miyamura, H.; Kobayashi, S.; Chechik, V. Spin Trapping of Au−H Intermediate in the Alcohol Oxidation by Supported and Unsupported Gold Catalysts. *J. Am. Chem. Soc.* **2009**, *131*, 7189−7196.
(58) Abad, A.; Corma, A.; García, H. Catalyst Parameters Determining Activity and Selectivity of Supported Gold Nanoparticles for the Aerobic Oxidation of Alcohols: The Molecular Reaction Mechanism. *Chem. - Eur. J.* **2008**, *14*, 212−222.
(59) Fristrup, P.; Johansen, L. B.; Christensen, C. H. Mechanistic Investigation of the Gold-Catalyzed Aerobic Oxidation of Alcohols. *Catal. Lett.* **2008**, *120*, 184−190.
(60) Zope, B. N.; Hibbitts, D. D.; Neurock, M.; Davis, R. J. Reactivity of the Gold/Water Interface During Selective Oxidation Catalysis. *Science* **2010**, *330*, 74−78.
(61) Kumar, G.; Tibbitts, L.; Newell, J.; Panthi, B.; Mukhopadhyay, A.; Rioux, R. M.; Pursell, C. J.; Janik, M.; Chandler, B. D. Evaluating Differences in the Active-Site Electronics of Supported Au Nanoparticle Catalysts Using Hammett and DFT Studies. *Nat. Chem.* **2018**, *10*, 268−274.
(62) Muñoz-Santiburcio, D.; Camellone, M. F.; Marx, D. Solvation-Induced Changes in the Mechanism of Alcohol Oxidation at Gold/Titania Nanocatalysts in the Aqueous Phase versus Gas Phase. *Angew. Chem., Int. Ed.* **2018**, *57*, 3327−3331.
(63) Mahdavi-Shakib, A.; Sempel, J.; Babb, L.; Oza, A.; Hoffman, M.; Whittaker, T. N.; Chandler, B. D.; Austin, R. N. Combining Benzyl Alcohol Oxidation Saturation Kinetics and Hammett Studies as Mechanistic Tools for Examining Supported Metal Catalysts. *ACS Catal.* **2020**, *10*, 10207−10215.
(64) Mori, K.; Hara, T.; Mizugaki, T.; Ebitani, K.; Kaneda, K. Hydroxyapatite-Supported Palladium Nanoclusters: A Highly Active Heterogeneous Catalyst for Selective Oxidation of Alcohols by Use of Molecular Oxygen. *J. Am. Chem. Soc.* **2004**, *126*, 10657−10666.
(65) Ato, Y.; Hayashi, A.; Koga, H.; Kawakami, T.; Yamanaka, S.; Okumura, M. Theoretical Study of Aerobic Oxidation of Alcohols over Au_{38} Nanocluster by a Two-Step-Modeling Approach. *Chem. Phys. Lett.* **2019**, *724*, 115−121.
(66) Schneider, C.; Rasband, W.; Eliceiri, K. NIH Image to ImageJ: 25 Years of Image Analysis. *Nat. Methods* **2012**, *9*, 671−675.
(67) Frisch, M. J.; Trucks, G. W.; Schlegel, H. B.; Scuseria, G. E.; Robb, M. A.; Cheeseman, J. R.; Scalmani, G.; Barone, V.; Mennucci, B.; Petersson, G. A.; Nakatsuji, H.; Caricato, M.; Li, X.; Hratchian, H. P.; Izmaylov, A. F.; Bloino, J.; Zheng, G.; Sonnenberg, J. L.; Hada, M.; Ehara, M.; Toyota, K.; Fukuda, R.; Hasegawa, J.; Ishida, M.; Nakajima, T.; Honda, Y.; Kitao, O.; Nakai, H.; Vreven, T.; Montgomery, J. A., Jr.; Peralta, J. E.; Ogliaro, F.; Bearpark, M.; Heyd, J. J.; Brothers, E.; Kudin, K. N.; Staroverov, V. N.; Keith, T.; Kobayashi, R.; Normand, J.; Raghavachari, K.; Rendell, A.; Burant, J. C.; Iyengar, S. S.; Tomasi, J.; Cossi, M.; Rega, N.; Millam, J. M.; Klene, M.; Knox, J. E.; Cross, J. B.; Bakken, V.; Adamo, C.; Jaramillo, J.; Gomperts, R.; Stratmann, R. E.; Yazyev, O.; Austin, A. J.; Cammi, R.; Pomelli, C.; Ochterski, J. W.; Martin, R. L.; Morokuma, K.; Zakrzewski, V. G.; Voth, G. A.; Salvador, P.; Dannenberg, J. J.; Dapprich, S.; Daniels, A. D.; Farkas, O.; Foresman, J. B.; Ortiz, J. V.; Cioslowski, J.; Fox, D. J. *Gaussian 09*; Gaussian, Inc.: Wallingford, CT, 2009.
(68) Lee, C.; Yang, W.; Parr, R. G. Development of the Colle-Salvetti Correlation-Energy Formula into a Functional of the Electron Density. *Phys. Rev. B: Condens. Matter Mater. Phys.* **1988**, *37*, 785.
(69) Becke, A. D. Density-Functional Thermochemistry. III. The Role of Exact Exchange. *J. Chem. Phys.* **1993**, *98*, 5648−5652.
(70) Luo, C.; Fa, W.; Dong, J. Adsorption of O_2 on Tubelike Au_{24} and Au_{24}^- Clusters. *J. Chem. Phys.* **2006**, *125*, 084707.
(71) Nhat, P. V.; Si, N. T.; Nguyen, M. T. Structural Evolution and Stability Trend of Small-Sized Gold Clusters Au_n (n = 20−30). *J. Phys. Chem. A* **2020**, *124*, 1289−1299.
(72) Matsuo, A.; Hasegawa, S.; Takano, S.; Tsukuda, T. Electron-Rich Gold Clusters Stabilized by Polyvinylpyridines as Robust and Active Oxidation Catalysts. *Langmuir* **2020**, *36*, 7844−7849.
(73) Hosokawa, F.; Shinkawa, T.; Arai, Y.; Sannomiya, T. Benchmark Test of Accelerated Multi-Slice Simulation by GPGPU. *Ultramicroscopy* **2015**, *158*, 56−64.
(74) Kamei, K.; Shimizu, T.; Harano, K.; Nakamura, E. Aryl Radical Addition to Curvatures of Carbon Nanohorns for Single-Molecule-Level Molecular Imaging. *Bull. Chem. Soc. Jpn.* **2020**, *93*, 1603−1608.
(75) Gorgoll, R. M.; Yücelen, E.; Kumamoto, A.; Shibata, N.; Harano, K.; Nakamura, E. Electron Microscopic Observation of Selective Excitation of Conformational Change of a Single Organic Molecule. *J. Am. Chem. Soc.* **2015**, *137*, 3474−3477.
(76) Du, K.; von Hochmeister, K.; Phillipp, F. Quantitative Comparison of Image Contrast and Pattern between Experimental and Simulated High-Resolution Transmission Electron Micrographs. *Ultramicroscopy* **2007**, *107*, 281−292.

https://doi.org/10.1021/jacsau.1c00102
JACS Au 2021, 1, 660−668